5-2012

Procedures for Correcting Digital Camera Imagery Acquired by the AggieAir Remote Sensing Platform

Shannon R. Clemens
Utah State University

PROCEDURES FOR CORRECTING DIGITAL CAMERA IMAGERY ACQUIRED BY THE AGGIEAIR REMOTE SENSING PLATFORM

by

Shannon R. Clemens

Thesis submitted in partial fulfillment of the requirements for the degree

of

WATER RESOURCE ENGINEERING

in

Civil and Environmental Engineering Department

Approved:

Thesis/Project Advisor Dr. Mac McKee	Committee Member Dr. Jeffery S. Horsburgh

Committee Member
Dr. Joseph Wheaton

UTAH STATE UNIVERSITY
Logan, UT

Spring 2012

CONTENTS

ABSTRACT

Procedures for Correcting Digital Camera Imagery

Acquired by the AggieAir Remote Sensing Platform

by

Shannon R. Clemens, Master of Science

Utah State University, 2012

Major Professor: Dr. Mac McKee
Department: Civil and Environmental Engineering

Developments in sensor technologies have made consumer-grade digital cameras one of the more recent tools in remote sensing applications. Consumer-grade digital cameras have been the imaging sensor of choice by researchers due to their small size, light weight, limited power requirements, and their potential to store hundreds of images (Hardin 2011). Several studies have focused on the use of digital cameras and their efficacy in remote sensing applications. For satellite and airborne multispectral imaging systems, there is a well established radiometric processing approach. However, radiometric processing lines for digital cameras are currently being researched.

The goal of this report is to describe an absolute method of radiometric normalization that converts digital numbers output by the camera to reflectance values that can be used for remote sensing applications. This process is used at the AggieAir Flying Circus (AAFC), a service center at the Utah Water Research Laboratory at Utah State University. The AAFC is a research unit that specializes in the acquisition, processing, and interpretation of aerial imagery obtained with the AggieAir™ platform. AggieAir is an autonomous, unmanned aerial vehicle system that

captures multi-temporal and multispectral high resolution imagery for the production of orthorectified mosaics. The procedure used by the AAFC is based on methods adapted from Miura and Huete (2009), Crowther (1992) and Neale and Crowther (1994) for imagery acquired with Canon PowerShot SX100 cameras. Absolute normalization requires ground measurements at the time the imagery is acquired. In this study, a barium sulfate reflectance panel with absolute reflectance is used. The procedure was demonstrated using imagery captured from a wetland near Pleasant Grove, Utah, that is managed by the Utah Department of Transportation.

(58 pages)

PUBLIC ABSTRACT

Procedures for Correcting Digital Camera Imagery Acquired by the AggieAir Remote Sensing Platform

Developments in sensor technologies have made consumer-grade digital cameras one of the more recent tools in remote sensing applications. Consumer-grade digital cameras have been the imaging sensor of choice by researchers due to their small size, light weight, limited power requirements, and their potential to store hundreds of images (Hardin 2011). Several studies have focused on the use of digital cameras and their efficacy in remote sensing applications. For satellite and airborne multispectral imaging systems, there is a well established radiometric processing approach. However, however the radiometric processing approach for digital cameras is still being researched.

The goal of this report is to describe an absolute method of radiometric normalization that converts digital numbers output by a camera to reflectance values that can be used for remote sensing applications. This process is used at the AggieAir Flying Circus (AAFC), a service center at the Utah Water Research Laboratory at Utah State University. The AAFC is a research unit that specializes in the acquisition, processing, and interpretation of aerial imagery obtained with the AggieAir™ platform. AggieAir is an autonomous, unmanned aerial vehicle system that captures multi-temporal and multispectral high resolution imagery for the production of orthorectified mosaics. The procedure used by the AAFC is based on methods adapted from Miura and Huete (2009), Crowther (1992) and Neale and Crowther (1994) for imagery acquired with Canon PowerShot SX100 cameras. Absolute normalization requires ground measurements at the time the imagery is acquired. In this study, a barium sulfate reflectance panel with absolute reflectance is used. The procedure was demonstrated using imagery captured from a wetland near Pleasant Grove, Utah, that is managed by the Utah Department of Transportation.

The results and accuracy of the supervised classification study using the converted reflectance value mosaics are discussed in this report. Also included are overall recommendations on the use of digital cameras and the processing of digital data to aim for higher quality results. The method and calculations used here can be used with other digital cameras along with the use of a reflectance white panel.

ACKNOWLEDGMENTS

I would like to thank Dr. Mac McKee and Dr. Thomas B Hardy for their encouragement to pursue a degree while working at the Utah Water Research Lab. I am grateful for the existence of the UWRL Scholarship and for the Scholarship Committee for choosing me as a recipient of these awards. It has been extremely helpful.

Lastly, I would like to thank my fiancé Erik Syrstad for his love, encouragement and support through this endeavor.

Shannon R. Clemens

LIST OF TABLES

LIST OF FIGURES

INTRODUCTION

Developments in sensor technologies have made consumer-grade digital cameras one of the more recent tools in remote sensing applications. Consumer-grade digital cameras have been the imaging sensor of choice by researchers for various applications such as wetland management, crop and biomass estimation, emergency response, civil and riparian studies due to their small size, lightweight, limited power requirements, and their potential to store hundreds of images (Hardin 2011). Several studies have focused on the use of digital cameras and their efficacy in remote sensing applications (Dean et al. 2000, Nebiker et al. 2008, Lebourgeois et al. 2008, Sakamoto et al. 2010, Levin et al. 2005). For satellite multispectral imaging systems, there is a well established radiometric processing approach. Manufacturers of satellite photogrammetric sensors have established laboratory-based calibration approaches for radiometry. However, these standards are not directly applicable in small format photogrammetric work flow due to the condition features of data acquisition (Honkavaara 2009). Photogrammetric sensors have a large field of view, which highlights bidirectional reflectance distribution function (BRDF) effects. In addition, image blocks are usually set with 20-80% overlap of images, which provides multiple views of the same ground object. Due to the high productivity requirements, digital imagery collection is not always carried out in optimal conditions. Radiometric approaches for digital cameras are a current research topic.

A digital imaging sensor, such as a charge-coupled device (CCD) or complementary metal–oxide–semiconductor (CMOS) camera, measures incoming radiance and stores the resulting measurement as a digital number (DN) from 0-255. Most digital cameras use a Bayer pattern array of filters to obtain red, green and blue bands for a digital image (Berni et al. 2009). The radiation that enters the imaging sensor is controlled by the aperture and exposure time

(Honkavaara et al. 2009a). Ideally, radiance is recorded by a system in various bands is an accurate representation of the radiance actually leaving the surface of interest (land, soil, water). However, internal and external noise error is inevitable and should be corrected. There are several factors that affect the signal and the conversion between object luminance and digital image measurement. Factors that are camera related are vignetting (fall off brightness on an image frame), camera settings such as International Organization for Standardization sensitivity value (ISO) and aperture, and color processing algorithms. Factors that are environmental include the angle of the sun, flight altitude and atmospheric conditions (Lebourgeois 2008).

Consumer-grade digital camera manufacturers customarily do not provide sensor or spectral band information. There are few reflectance conversion methods available which can be used with consumer-grade digital cameras, none of which are considered the standardize method for conversion. Reflectance values are dimensionless. The reflectance is "the ratio of the radiant flux reflected by a surface to that reflected into the same reflected-beam geometry by an ideal, perfectly diffused standard surface irradiated under the same conditions" (Nicodemus et al. 1977), or the fraction of electromagnetic radiation which was reflected by the surface being analyzed.

Some strategies use only information drawn from the image, while other strategies required varying degrees of information of the surface reflectance properties at the time the imagery was acquired. The empirical line method is used by several searchers in conjunction with digital cameras (Dean et al. 2000, Berni et al. 2009, Levin et al. 2005). Empirical line method requires field reflectance spectra to be acquired from uniform ground target areas which could be challenging with remote flight locations. Other researchers performed analysis using digital numbers – in calibrated or uncalibrated – to perform vegetation index studies (Nebiker et al.

2008, Sakamoto et al. 2010, Lebourgeois et al. 2008, Swain et al.). Using digital numbers may not provide the complete spectral depth required for analysis.

The goal of this report is to describe an absolute method of radiometric normalization that converts digital numbers to reflectance values. This process is used at the AggieAir Flying Circus (AAFC), a service center at the Utah Water Research Laboratory at Utah State University. The AAFC is a research unit that specializes in the acquisition, processing, and interpretation of aerial imagery obtained with the AggieAir^{TM} platform. AggieAir is an autonomous, unmanned aerial vehicle (UAV) system, which captures multi-temporal and multispectral high resolution imagery for the creation of orthorectified mosaics. The procedure is based on methods adapted from Miura and Huete (2009), Crowther (1992) and Neale and Crowther (1994) for imagery acquired with the AggieAir platform. Absolute normalization requires ground measurements at the time the imagery is acquired. In the study described in this report, a barium sulfate reflectance panel with absolute reflectance was used. The procedure was demonstrated using imagery captured from the Utah Lake Wetlands Mitigation Bank near Pleasant Grove, Utah, which is managed by the Utah Department of Transportation.

PREVIOUS WORK – LITERATURE REVIEW

The research of general digital imagery and its use in spectrally quantitative applications is a current topic. In May 2008, the European Spatial Data Research organization (EuroSDR) launched a project for the purpose of improving the knowledge of radiometric aspects of digital photogrammetric airborne images, mostly large-format sensors, to review the existing methods for radiometric image processing, and to analyze the benefits of radiometric calibration in

different applications such as quantitative remote sensing, land classification and change detection studies (Honkavaara et al. 2009a).

The EuroSDR project was launched in two phases. Phase 1, which completed in 2009, was a review of state of the art and theoretical radiometric aspects of digital photogrammetric images from various mapping sensors (Honkavaara et al. 2009b). The report included results from a survey from National Mapping Agencies and universities on large-format digital imagery. The main conclusions were that improvements were needed for the entire correction process: sensors, calibration, data collection, data post-processing, and data utilization. The radiometric processing lines were inadequate and standards were missing (methods, calibration, reference targets, and terminology). Phase 2 (Honkavaara et al. 2011) was a comparative, multi-site, empirical investigation on large-format photogrammetric imagery using various correction methods. Although the typical application areas of small- and medium-format sensors are different from large-format sensors, the results of this project may aide in the progress of small- and medium-format processing lines and demonstrate the need for current research on this topic.

Several researchers have explored the capabilities of small-format digital cameras for remote sensing purposes while dealing with common issues that digital cameras present. Dean et al. (2000) presented an empirical method for correcting brightness fall-off due to vignetting effects and increasing view angles by treating bands individually for a Kodak DSC460c digital camera with color visual (RGB) and color-infrared (CIR) bands. For a Kodak DCS460c, Dean et al. (2000) found that raw images in digital numbers are most reliable when comparing spectral values quantitatively. Dean et al. also suggest that digital numbers can only be converted to reflectance after images are corrected for topographically induced variations in intensity and for bidirectional reflectance distribution function.

Berni et al. (2009) used the empirical line method to spectrally calibrate a commercialized camera called Tetracam (MCA-6, Tetracam, Inc., CA), a low-cost multispectral (6 band) digital camera, which was onboard a UAV helicopter. With this imagery, various vegetation indices were calculated on various agricultural fields, including leaf area index. Calibrated reflectance imagery was then validated in the field with spectral measurements. They also used a thermal band camera, for which atmospheric effects on transmittance were evident, even at low altitudes. Atmospheric correction methods based on MODerate resolution atmospheric TRANsmission (MODTRAN) radiative transfer model were used to estimate surface temperatures.

Nebiker et al. (2008) used a micro-UAV (under 5kg) with a Canon EOS 20D commercial digital single-lens reflex (SLR) camera with a CMOS chip for the (RGB) sensor and a Sony SmartCam CCD digital camera for the NIR sensor. Uncalibrated or raw digital numbers were used to calculate normalized differential vegetation indices (NDVI), which located stressed plants. Leaf damage ground truth samples were collected and were matched to the NDVI values by means of a weighted linear regression. Good success was reported when using simple raw pixel values.

Swain et al. (2010) used remote controlled helicopters equipped with a CMOS Tetracam multispectral digital camera to estimate yield and total biomass of a rice crop. They used raw, uncalibrated digital numbers to calculate NDVI rather than reflectance factors. These were calculated with Pixelwrench, a software that derived vegetation indices from raw image data. No georeferencing or rectification was performed. A field spectrometer was used to collect ground-based readings in conjunction with a barium sulfate white panel. Their results showed an $R^2 = 0.897$ fit between NDVI values of the spectrometer and NDVI of the Tetracam imagery.

Lebourgeois et al. (2008) studied JPEG and RAW (CR2 Canon) image formats in combinations of corrected and non-corrected images to test for quantitative surface parameter results such a vegetation indices. Many studies have focused on image geometry from digital camera imagery, but not as much attention has been given to the relationship between pixel values and target radiance (Kuusk and Paas, 2007). Lebourgeois et al. (2008) used three Canon EOS 400D digital cameras – visual color (RGB), near-infrared (NIR), and red-edge (RDG) cameras. The NIR and RDG cameras were equipped with high-pass and external band-pass filters to acquire these spectral ranges. The spectral ranges of all the cameras were measured in a laboratory. The aperture and shutter speed were adjusted manually to avoid oversaturation. Lebourgeois et al. (2008) decoded the RAW (CR2 format for Canon) images using a free web software Buil C (http://www.astroturf.com/buil/iris/iris.htm) and compared it to the JPEGs. However, due to the different image sizes, the RAW and JPG digital numbers, and different value depths (12 bit versus 8 bit respectively), they could not be directly compared. Because of this, light and dark or invariant objects were used for comparison instead. The results showed that JPG and decoded RAW were not linearly related.

Different sets of vegetation indices were created for comparison: $NDVI_{jpeg}$ (unprocessed JPG), $NDVI_{raw}$ (RAW CR2 imagery), $NDVI_{raw\_dev}$ (RAW imagery decoded and vignetting corrected), and $NDVI_{raw\_dev\_norm}$ (RAW imagery decoded, vignetting corrected, and normalized). Although Lebourgeois et al. (2008) compared invariant and cosine normalization methods, they also mentioned the simplest and most commonly used method of normalization, called the "normalized brightness values". This was used to normalize imagery (Crimmins and Crimmins 2008; Richardson et al 2007). A vignetting correction method was also applied to the latter set of data by fitting a polynomial function distribution on an average image.

Lebourgeois et al. (2008) found no clear advantage between $NDVI_{jpeg}$, $NDVI_{raw}$, $NDVI_{raw\_dev\_norm}$. However, the $NDVI_{raw\_dev}$ (RAW imagery decoded and vignetting corrected) showed a slightly better result. They conclude that vignetting correction most significantly improves the quality of the vegetations indices when red, green and NIR bands are used. If only red and green bands were used, the vignetting corrections were less evident. This was most likely due to the fact that NIR and RGB come from two cameras with individual vignetting effects. The relationship between raw JPG and RAW was shown to be non-linear. This was because (1) the digital numbers of vegetation were low in the RGB and NIR, which were positioned in the linear part of the gamma correction function of the camera, and (2) the digital numbers were calculated on a polygon basis and the spatial interpolation of the JPEG did not affect the mean radiometric value. If high radiometric values were the targets, the conclusions would be different, however, and a significant result of the RAW correction would be evident.

Sakamoto et al. (2012) used two Nikon COOLPIX P5100 digital cameras, an RGB and NIR with band-pass filter (830 nm), in a crop phenology recording system (CPRS) to capture hourly imagery that was used to perform quantitative monitoring of maize and soybean. Moderate-resolution Imaging Spectroradiometer (MODIS) satellite data and a four-channel radiometer SKYE measured crop reflectance to validate the results. Vegetation indices were calculated from calibrated digital numbers. The gamma characteristic, the nonlinear relationship between the digital number and the incident light intensity, was calibrated using a formula derived from a laboratory experiment. Any calibration digital number under 100 was linear with light intensity, and therefore an hourly average was derived for each channel. Vegetation indices were calculated from calibrated digital numbers and compared to calculated vegetation indices from spectral reflectance observations from the crop sensor and MODIS imagery. The

vegetation indices derived from the daytime camera showed close resemblance to the calculated vegetation indices.

Levin et al. (2005) used an Olympus CAMEDIA C-920 digital camera as tool to measure color indices and properties of soils in arid environments. Rather than having the camera on-board a UAV, they mounted the camera looking downward over a fixed area on the ground. The 8-bit digital numbers were saved in JPG format and processed using ENVI software (Research Systems 2000). Digital numbers were calibrated using relative and absolute methods. The relative methods involved a linear regression between RGB values of colored chips placed on the ground which were corrected to match conditions of the base image. The absolute calibration of reflectance values was based on spectral reflectance of the color chips using a field spectrometer where an exponential regression line was found between digital numbers and measured reflectance values of the colored chips.

Miura and Huete (2009) compared three reflectance calibration methods for airborne hyperspectral spectrometer data to reflectance factors using an Olympus C3000 digital camera. The first was a "reflectance mode" method, which calibrates a spectrometer against a white panel and then mounts the spectrometer on an aircraft. This lead to biased results based in converted reflectance data and distortion due to flight length and time of day. The second was a "linear interpolation" method, which converts airborne spectrometry data by taking a ratio of linearly interpolated reference values from pre- and post-flight white panel readings. The results of this method, while precise, were inaccurate, but had no distortion. The third was a "continuous panel" method, which uses a radiometer to obtain continuous measurements over a reflectance panel throughout the flight in order to adjust the degree of the linear interpolated reference values from pre- and post-flight white panel readings. This method was the only method from

this paper that collected unbiased reflectance factors and consistently derived accurate, unbiased reflectance factors. It was ideal for flights during any time of the day and long flights as well (1-2 hours).

As the literature shows, there is a need for radiometric and reflectance calibration processing lines that could apply to all consumer-grade digital cameras. Researchers often used the empirical line method for reflectance conversions or used digital numbers. They systems and sensors used vary greatly so a processing chain that is applicable for various systems proves to be a challenge. This paper discusses a protocol for a consumer-grade digital camera which could be applicable for other small-format photogrammetric sensors. This paper discusses a "reflectance mode" method from Miura and Huete (2009) with modifications aimed at reducing the reflectance value conversion bias. AAFC captures a post-flight white panel photo using the same camera used for the mission and a calibrated white panel with known reflectance properties rather than a spectrometer. The method requires little equipment while in the field and is applicable to other consumer-grade digital cameras.

MATERIALS

UAV and Payload Description

AggieAir is an autonomous, low cost unmanned aerial vehicle (UAV) system developed by the Center for Self Organization and Intelligent Systems (CSOIS) and the Utah Water Research Laboratory (UWRL) at Utah State University (USU) (see Figure 1). AggieAir is a two-camera system with spectral bands in the red, green, blue and near-infrared portions of the electromagnetic spectrum. AggieAir requires no runway or landing pad to operate. An onboard GPS system records the location and position of each image frame, with images taken every four

seconds while the UAV is in flight. An inertial measurement unit (IMU) records the yaw, pitch and roll of the UAV, which are critical in the mosaicking process. Table 1 lists other specifications of the AggieAir UAV (Jensen et al. 2009).

Figure 1. AggieAir's unmanned aerial vehicles (UAV) used for the UDOT wetlands mission

Table 1. AggieAir aircraft specifications

Details	Specifications
Wingspan	1.8 m (72 in)
Weight	3.62 kg (8 lbs)
Nominal Air Speed	15 m/s (33 mph)
Max flight duration	45 min - 1 hour
Battery capacity	16,000 mAh
Payload capacity	1.36 kg (3 lbs)

Digital Cameras

The RGB digital camera used by AggieAir is a Canon PowerShot SX100, which has a 9-megapixel CCD sensor and an ISO range from 80 to 1600. The PowerShot records in 8-bit

color, with digital numbers ranging from 0-255 and an image size of 3264 x 2248 pixels. The NIR camera is also a Canon PowerShot SX100 having similar specifications, but with a RGB bandpass filter that was removed and replaced with a Wratten 87 NIR filter that allows NIR wavelengths of 750 nm (Figure 2). Table 2 provides additional camera specifications.

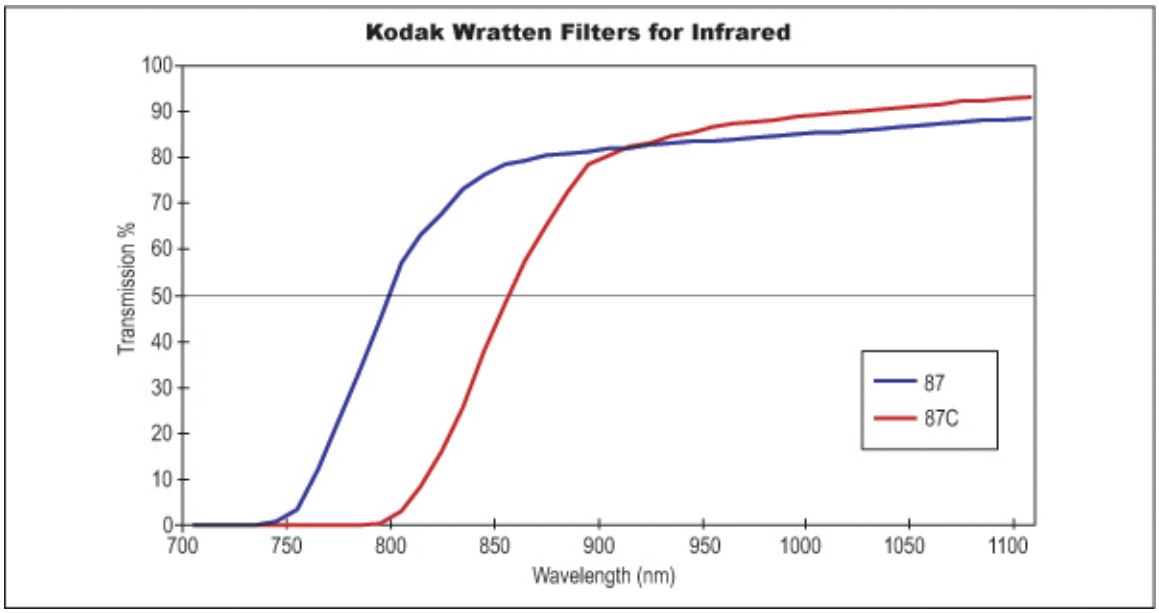

Figure 2. The NIR wavelength shown in blue (750 nm) of the NIR camera after a Kodak Wratten filter is added (MaxMax, LLC, Carlstadt, NJ, USA)

Table 2. Camera specifications for Canon PowerShot SX100

Details	**Specifications**
Resolution	3264 x 2248 pixels
Focal Length	6 mm
Field of View	50 x 39 degrees
Time Between Images	4 secconds
Weight	250 grams

The specific spectral characteristic of the imaging element for the red, green and blue band are not disclosed by Canon at this time. Currently, it is assumed that the Canon has a typical unfiltered CDC/CMOS spectral response curve as shown in Figure 3.

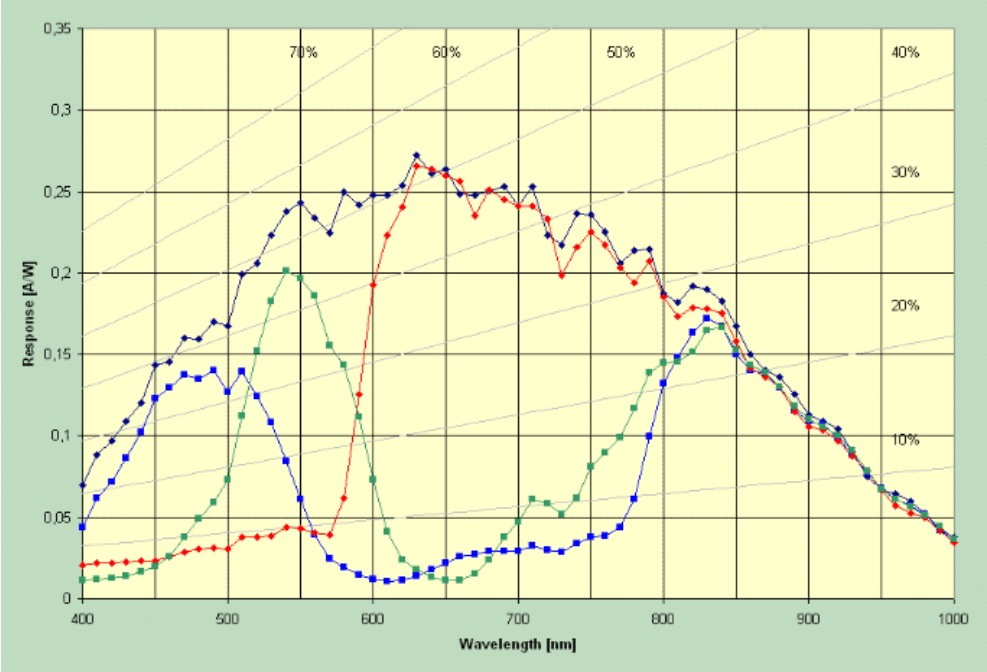

Figure 3. A typical unfiltered CCD/CMOS spectral response curve for each of the red, green and blue pixels. The top dark blue plot shows the quantum efficiency (MaxMax, LLC, Carlstadt, NJ, USA).

Reflectance Panel and Neutral Density Filters

A near-Lambertian white reflectance panel from Labsphere, Inc. was used in the field before and after a UAV flight mission was performed by the AggieAir Flying Circus. The 24 inch white panel was made of a barium sulfate-based formulation that has a reflectance of 95-98% (Labsphere, Inc., North Sutton, NH, USA). The white panel was then spectrally calibrated

against a Halon reflectance panel with manufacturer supplied reflectance coefficients using different sun zenith angles.

Photos of the white panel were taken in the field before and after a UAV flight using the same RGB and NIR cameras that were used on the UAV. To eliminate flux and brightness cues caused by overexposure of the white panel, a Kodak neutral density filter with a known transmittance was placed in front of the RGB lens. Filters from 0.1 to 0.9 represent the amount of transmitted light through the filter created by a uniformly bright surface. A filter was selected that allows for the most suitable histogram distribution. The neutral density filters were used during post-processing when calculating the fractional transmittance.

Study Site

AggieAir flew a 3.18 km^2 (1.23 mi^2) section of a wetland near Pleasant Grove, Utah for the Utah Department of Transportation (UDOT) on August 24, 2011. Both RGB and NIR imagery were collected. The UAV flight captured 161 RGB and 161 NIR JPG images between 9:38 am and 9:50 am.

Ground Truthing Sampling

UDOT field crews collected ground truth sample points of known wetland species with a Global Positioning Service (GPS) on August 15, 2011 (see Figure 4). The horizontal precision of the GPS points ranged from 0.662 to 2.412 meters with an average of 1.058 meters; and the vertical precision of the points ranged from 0.827 to 3.079 meters with an average of 1.475 meters. UDOT also provided at a later date hand drawn polygons identified as new wetland species for the data set after the initial wetland species classification results with hopes to

improve future results. The plant species that were identified and mapped were *Agrostis*, Baltic rush, beaked sedge, cattail (narrowleaf, broadleaf and new), hardstem bulrush, *Phragmites* (old and new) and saltgrass. See **Error! Reference source not found.** for a map of the ground truth data of the GPS and polygon wetland species.

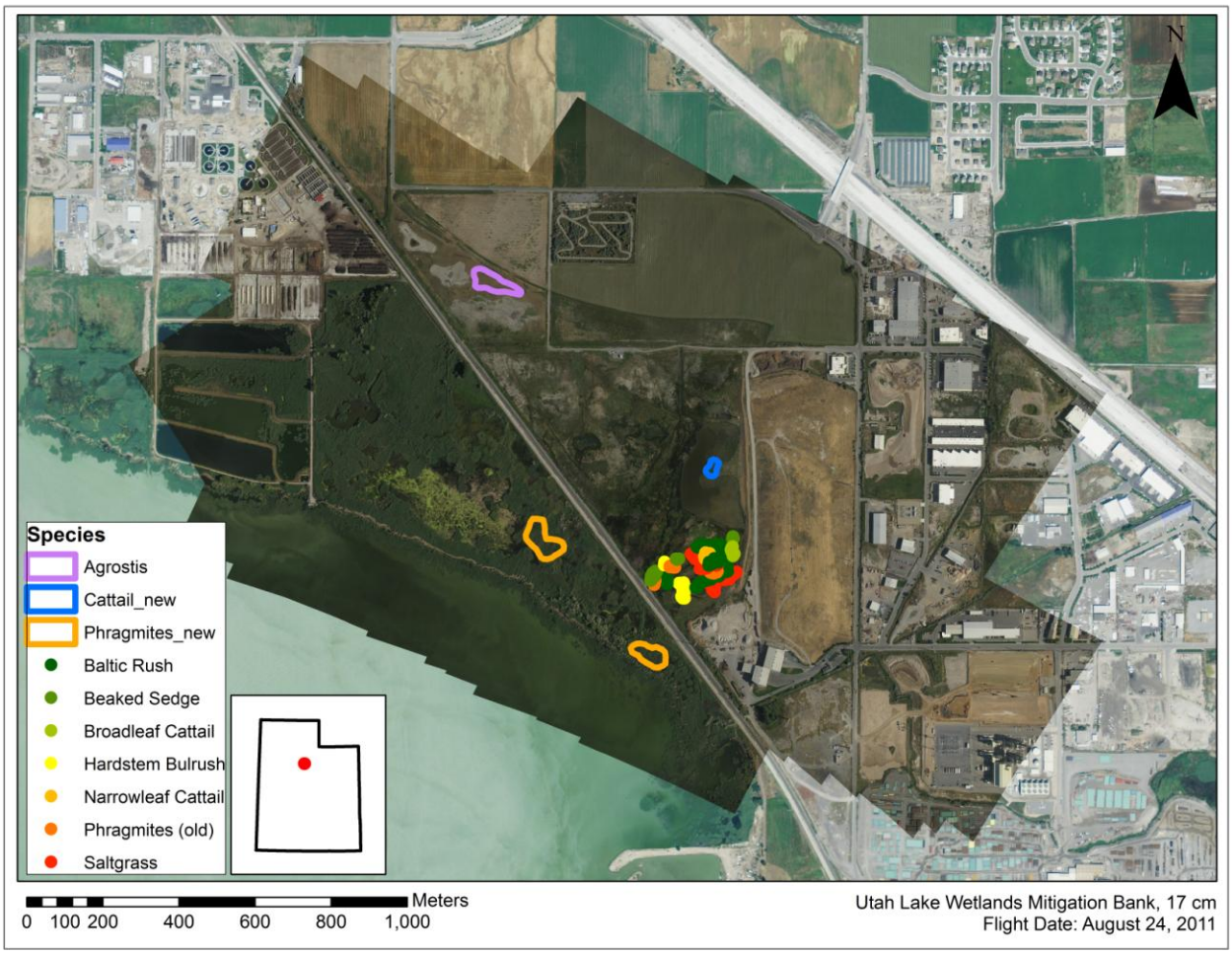

Figure 4. Map of ground truth polygons and GPS points from UDOT field crews with the RGB imagery from August 2011 for the background

METHODOLOGY

The method used for absolute radiometric normalization of AggieAir imagery was adapted from Miura and Huete (2009), Crowther (1992) and Neale and Crowther (1994). Dr. Bushra Zaman created ERDAS (Leica Geosystems Geospatial Imaging, LLC) models and an Excel spreadsheet to perform zenith angle calculations (Duffie and Beckman 1991). The "reflectance mode" method calibrates a spectrometer against a white panel then mounts the spectrometer on an aircraft. Equation 1 is the basis of the reflectance factor calculation of the "reflectance mode" method where DN_T and DN_R are the digital numbers from a spectrometer when viewing the target and reference at a specific time t; and R_R is the reflectance factor of the white panel which will determine R_T the reflectance factor of the unknown surface at zenith angle θ_t:

$$R_T(\theta_t) = \frac{DN_T(t)}{DN_R(t)} R_R(\theta_t) \quad (1)$$

The modifications made to this method by AAFC are the addition of an after-flight white panel photo, which is captured with the same camera used for the before-flight white panel photo and for the flight mission, using a reflectance panel with known reflectance coefficients. The objective was to derive correction functions that could be applied to the orthorectified mosaics in order to remove the irradiance variations and to convert digital numbers to reflectance values.

The current steps for converting orthorectified mosaics to reflectance values are: (1) generate RGB and NIR orthorectified mosaics from post flight imagery, (2) calculate the corrected brightness value for each spectral band of the reflectance panel photos, (3) calculate the reflectance factors for each spectral band for the reflectance panel, (4) calculate the reflectance images for individual bands using the orthorectified mosaics, and (5) perform layer stack on bands to create a final reflectance mosaic.

While in the field, the UAV field crew determined aperture and ISO settings before each flight based on the lighting conditions. These settings were specific to that particular flight at that particular time of day and camera. Lebourgeois (2008) indicated that most researchers use the automated settings on digital cameras to capture imagery in JPG or TIFF format. The image analysis can be qualitatively satisfactory, but the radiometric accuracy is usually too low for quantitative surface estimates under the automated settings. For this reason, aperture and ISO settings were manually chosen to avoid over or underexposing the images during flight. Crews manually set the camera so most of the pixels in the image are centered on the value 127 because it is between 0 and 255, which is the range of a pixel value. If the image is overexposed, many of the pixels will be at or around 255; if underexposed is the opposite. After the camera settings are chosen, the crew takes a photo of the white panel prior to the flight. The picture of the white panel the panel image would be overexposed because the panel is too bright. When the image is over- or underexpose, data is lost, so a neutral density filter is used in front of the lens keeping the same manual settings in order to eliminate flux and brightness cues. After the UAV landed, the NIR and RGB cameras were removed from the plane and after-flight white panel photos were captured once again. Images from the digital camera as well as GPS flight information were downloaded onto a laptop computer and examined so that spatial coverage of the area of interest could be verified.

The reflectance calculations were performed for each spectral band using Equation 2:

$$\boldsymbol{Reflectance\ Image}_{(x,y)} = \boldsymbol{Reflectance\ Factor}_{(a,c,f)} \times \left(\frac{\boldsymbol{Image}_{x,y(a,c,f)}}{\boldsymbol{CBV\ White\ Panel}_{(a,c,f)}} \right) \quad (2)$$

where the *reflectance factor* for each band is derived from the white panel photos based on the zenith angle of the sun, the *image* is the RGB or NIR orthorectified mosaic, and the *CBV white panel* is the scalar corrected brightness value to correct for vignetting, sensor non-uniformities

and angular deviation from nadir (Neale 1994) where *x,y* is the pixel acquired from camera *c* at aperture *a* with neutral density filter *f* (for RGB camera)**.**

Generate Orthorectified Mosaics

Images from the flight were uploaded to NASA World Wind, which is a customizable geographical information system. Flightlines were arranged by headings, and necessary flight images were exported for readability in EnsoMosaic UAV. EnsoMosaic UAV, developed by Mosaic Mill of Finland, is an image processing software that reads aerial images captured with compact digital cameras used onboard UAVs and processes them into seamless orthorectified image mosaics (MoasicMill Ltd, Finland). GPS information was collected for each individual image frame during the flight using a pre-set starting and stopping altitude, collecting XYZ coordinates for the center of each image. Separate projects were created within EnsoMosaic UAV to process RGB and NIR imagery because these images were acquired from separate cameras. In EnsoMosaic UAV, adjoining image pairs were manually linked together with common tie points between most image pairs. Next, automatic tie point iteration was run with large residuals removed manually.

After the number of tie points was sufficient between all image pairs, the bundle block adjustment (BBA) was run. BBA is an "iterative mathematical process to solve the orientation of the images and the location of the perspective centers simultaneously for a large image block" (MosaicMill User's Guide 2009: 2). After each iteration, an estimation of the global accuracy of the image rectification, called adjustment error, was reported. Adjustment error is the mean error of unit weight, a function of all the residuals and all the weights (MosaicMill User's Guide 2009: 43). After each round of the BBA, erroneous tie points with large residuals were manually

removed, and the BBA rerun. This continued until the largest residuals were deleted and the accuracy of the mosaic was considered satisfactory, which was when the total adjustment error was at its best.

After the BBA, a Digital Terrain Model (DTM) with 10 meter ground resolution was generated for orthocorrection of the mosaic (this is a default ground resolution which will be coarse). The DTM was created based on the elevation values generated for each tie point during the BBA (MosaicMill User's Guide 2009: 54). Lastly, the mosaics were created by rotating and rectifying each image to the ground coordinate system. The resulting mosaics had a pixel resolution of 17 centimeters.

Corrected Brightness Value

The corrected brightness value (*CBV*) is a calculated scalar image that is applied to each image acquired from the same camera and flight in order to correct for diminishing image irradiance from the center of the image, such as vignetting. The before- and after-flight white panel photos were used in the *CBV* calculation. The time and date of each photo was utilized in the sun angle calculations for the reflectance factors.

1. Visual Color Imagery - CBV

The RGB camera was used in conjunction with the best suited neutral density filter for the before- and after-flight white panel photos. Using an ERDAS model developed by Dr. Bushra Zaman**Error! Reference source not found.**, the RGB bands from the before flight white panel photo were separated in order to calculate the normalized brightness value (*NBV*), or the mean of the image pixel values, for the red, green and blue channels. The channels were

separated due to the unique response each band has to irradiance. Calculating the normalized brightness value is the simplest and most common normalization method (Crimmins and Crimmins 2008, Richardson et al. 2007).

After the normalized brightness value was calculated, a correction coefficient, *CC,* was calculated for each channel of the before-flight white panel photo by taking the normalized brightness value for that channel, $NBV_{(a,c,f)}$ (a scalar value), divided by the brightness value of each pixel for that channel $BV_{x,y(a,c,f)}$ where *x,y* indicates the pixel of that particular channel, *a* is the aperture, *c* is the camera, and *f* is the neutral density filter from which the imagery was acquired as seen in Equation 3:

$$\boldsymbol{CC_{x,y(a,c,f)} = \frac{NBV_{(a,c,f)}}{BV_{x,y(a,c,f)}}} \quad (3)$$

Once the correction coefficient was calculated for that band, aperture, and camera combination, the corrected brightness value was calculated. The *CBV* was the result of the correction coefficient, $CC_{x,y(a,c)}$, multiplied by the brightness value of a pixel on the before-flight white panel, $BV_{x,y(a,c),}$ divided by the transmittance factor, I/I_0, which is the percentage of light passing through the lens. The equation is:

$$\boldsymbol{CBV_{x,y(a,c)} = CC_{x,y(a,c)} \times \frac{BV_{x,y(a,c)}}{I/I_0}} \quad (4)$$

Here $I/I_0 = 10^{-d}$, where *d* is percent transmittance of the neutral density filter used in front of the RGB camera lens. A filter of *d = 0.2* recorded in the field means that 20% of the light was passing through the lens (see Table 3 for the various neutral density filters). If no filter was necessary then *d = 1*, meaning 100% of the light was passing through the lens. This is the transmittance factor, or fractional transmittance, where I_0 is the incident intensity radiation and *I* is the measureable intensity transmitted through the filter (Wikipedia), related to surface albedo.

The above process was repeated for the after-flight white panel image. The two resulting images were averaged to create a final corrected brightness value (scalar value) for the red, green and blue channels which correct for diminishing fall-off brightness due to non-nadir images, lens vignetting, and sensor non-uniformities (Neale 1994). Figure 5 through Figure 8 demonstrate how the correction coefficient was applied to correct the white panel image and the corrected brightness value using the ERDAS surface.

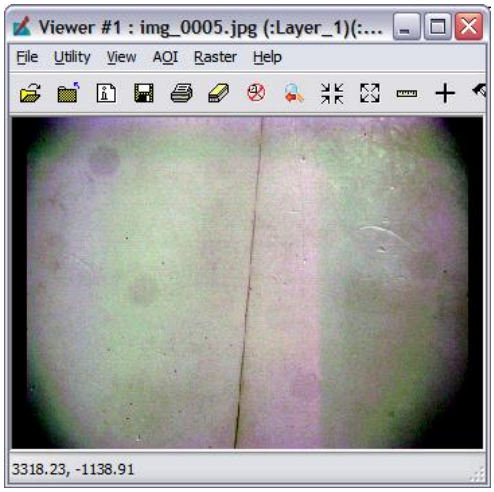

Figure 5. Raw white panel image in ERDAS viewer

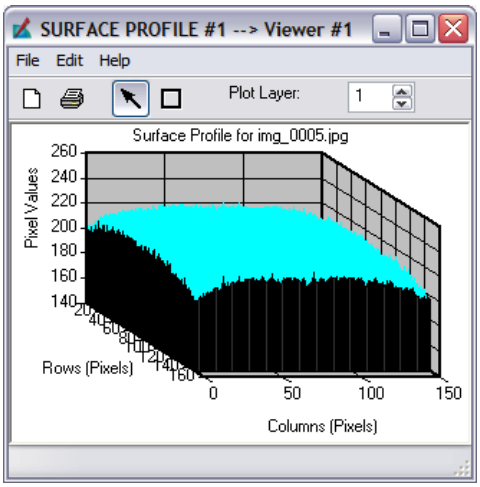

Figure 6. Raw white panel image opened in ERDAS surface profiler

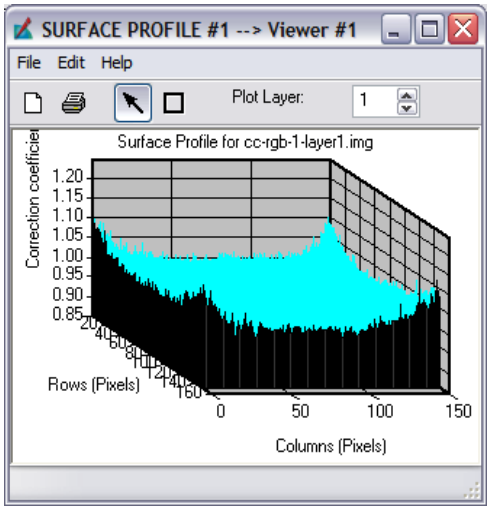

Figure 7. Surface profile of CC image

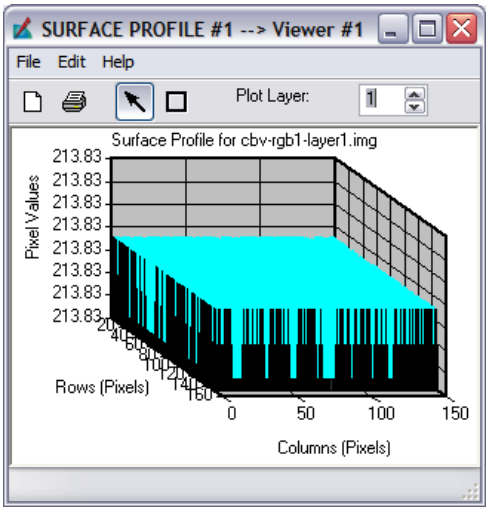

Figure 8. Corrected brightness value image opened in ERDAS surface profiler

Table 3. Various neutral density filters used with the barium sulfate white panel

Neutral Density Filter	I/I_0 value
0.1	0.7943
0.2	0.6310
0.3	0.5012
0.4	0.3981
0.5	0.3162
0.6	0.2512
0.7	0.1995
0.8	0.1585
0.9	0.1259
1.0	0.1000

2. Near Infrared Imagery - CBV

The corrected brightness value for the near infrared white panel image was calculated similarly to the RGB procedure. Although the RGB bandpass filter was removed and replaced with an NIR filter, the output of a CCD camera was still a three-band JPG in the red, green and blue spectra. The red band most closely resembled the NIR band spectrally and was used for the NIR models. This was extracted from the before-flight white panel image and averaged to represent the normalized brightness value. As stated for the RGB calculation, a correction coefficient, $CC_{x,y(a,c)}$, was calculated for the red channel by taking the normalized brightness value, $NBV_{(a,c)}$, divided by the brightness value of each pixel, $BV_{x,y(a,c)}$, where *a* is the aperture, and *c* is the camera, as seen in Equation 5:

$$\boldsymbol{CC_{x,y(a,c,f)} = \frac{NBV_{(a,c)}}{BV_{x,y(a,c)}}} \quad (5)$$

Since neutral density filters are not used on the NIR white panel images, the correction coefficient multiplied by the brightness value of each pixel, $BV_{x,y(a,c)}$ which equaled the corrected brightness value.

$$\boldsymbol{CBV_{x,y(a,c)} = CC_{x,y(a,c)} \times BV_{x,y(a,c)}} \quad (6)$$

This process was repeated for the after flight white panel image and the two resulting images were averaged to create a final corrected brightness value (scalar value) for the NIR (i.e., the red) layer that corrected for diminishing fall-off brightness due to non-nadir images, lens vignetting and sensor non-uniformities (Neale 1994) where *x*,*y* is the pixel acquired from camera *c* at aperture *a*.

White Panel Reflectance Factors

The third step was to calculate the reflectance factors of the barium sulfate white panel for the red, green, blue and NIR bands. The reflectance factors of the white panel were determined using the calibrated reflectance coefficients and the zenith angle of the sun, which uses data about the date and time of the before- and after-flight white panel images. The barium sulfate white panel was calibrated in-house to derive specific reflectance coefficients for each channel (see Table 4).

Equation 6 from *Remote Sensing of Land Surfaces* BIE 6250, a course at Utah State University, was used to calculate the reflectance factors:

$$\boldsymbol{R_{p\lambda} = A_0 + A_1 * (\theta_z) + A_2 * (\theta_z)^2 + A_3 * (\theta_z)^3 + A_4 + (\theta_z)^4} \quad (7)$$

where $R_{p\lambda}$ is the reflectance value of the panel, which is independent of illumination and incident light, and A_0, A_1, A_2, A_3 and A_4 are the reflectance coefficients of the panel that were used for calibration of the imagery. θ_z is the zenith angle of the sun, which was calculated for

the calendar date and time of photo. See the Appendix for a detailed explanation of the zenith angle calculations.

Table 4. Known reflectance coefficients of barium sulfate white panel

Band	A0	A1	A2	A3	A4
Green	1.099792	-0.00146	-0.000074	0.00000159	-0.000000012
Red	0.309000	0.13570	-0.004700	0.00006000	-0.000000300
NIR	1.290200	0.09500	-0.002800	0.00002000	-0.000000030
Blue	-0.049700	0.11940	-0.004400	0.00007000	-0.000000400

A zenith angle was calculated for the time of the before- and after-flight photos and averaged in order to derive a final reflectance factor to be used with each channel. Table 5 refers to the resulting reflectance factors of the white panel taken on August 24, 2011 at 9:10 am and 10:18 am at Local Longitude (Lon_{loc}) -111.77 and Local Latitude (Lat_{loc}) 40.34. An average assumes a linear relationship between the digital numbers and reflectances. This is assumed to be appropriate because of the inherently short duration of the UAV flight.

Table 5. Final reflectance factors of the August 24, 2011 flight

	NIR	RED	GREEN	BLUE
Reflectance Panel Image, before flight	1.214482	0.873758	0.957389	1.182844
Reflectance Panel Image, after flight	1.760020	1.251002	0.990410	1.143861
Final Reflectance Factors	1.487251	1.062380	0.973899	1.163353

Reflectance Images and Layer Stacking

The fourth step in the process involved the conversion of orthorectified mosaics of digital numbers to reflectance values. Referring back to the equation for a reflectance image, we now have the reflectance factors and the corrected brightness values needed for Equation 8:

$$\boldsymbol{Reflectance\ Image}_{(x,y)} = \boldsymbol{Reflectance\ Factor}_{(a,c,f)} \times \left(\frac{\boldsymbol{Image}_{x,y(a,c,f)}}{\boldsymbol{CBV\ White\ Panel}_{(a,c,f)}} \right) \quad (8)$$

1. RGB Reflectance Model

The RGB model used the orthorectified mosaic TIFF generated from EnsoMosaic as an input and separated the red, green and blue bands for analysis. Each of the bands were divided by their respective corrected brightness value and then multiplied by the reflectance factor specific to that channel (Eq. 8). The outputs of the RGB reflectance model were individual red, green and blue layers expressed as reflectance values. Red reflectance values ranged from 0.0035 to 1.0057, green reflectance values ranged from 0.0034 to 0.7722, and blue values ranged from 0.0024 to 0.9037. See Figure 9 through **Error! Reference source not found.** for individual reflectance images for the UDOT flight on August 24, 2011.

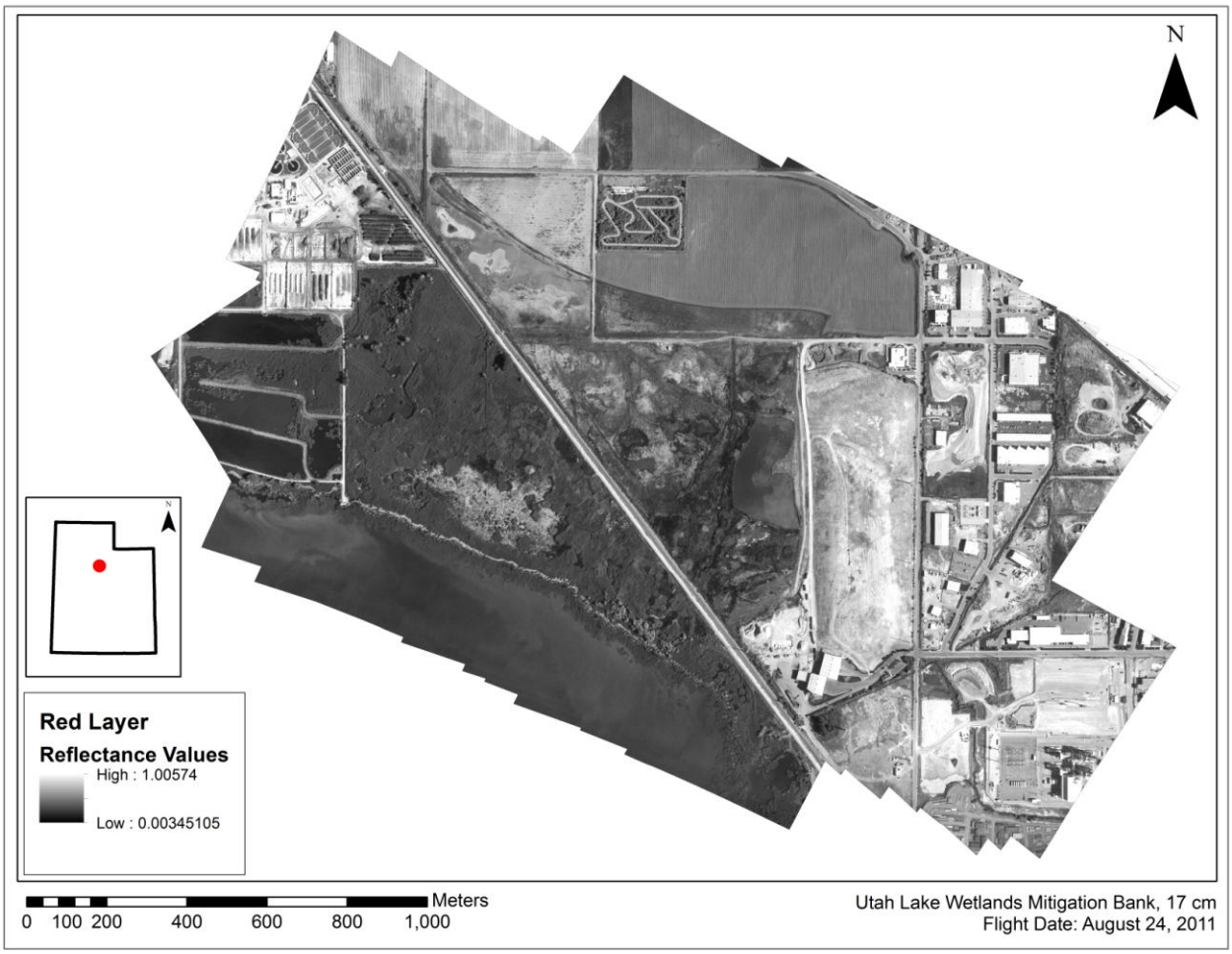

Figure 9. Red layer output from RGB reflectance value model

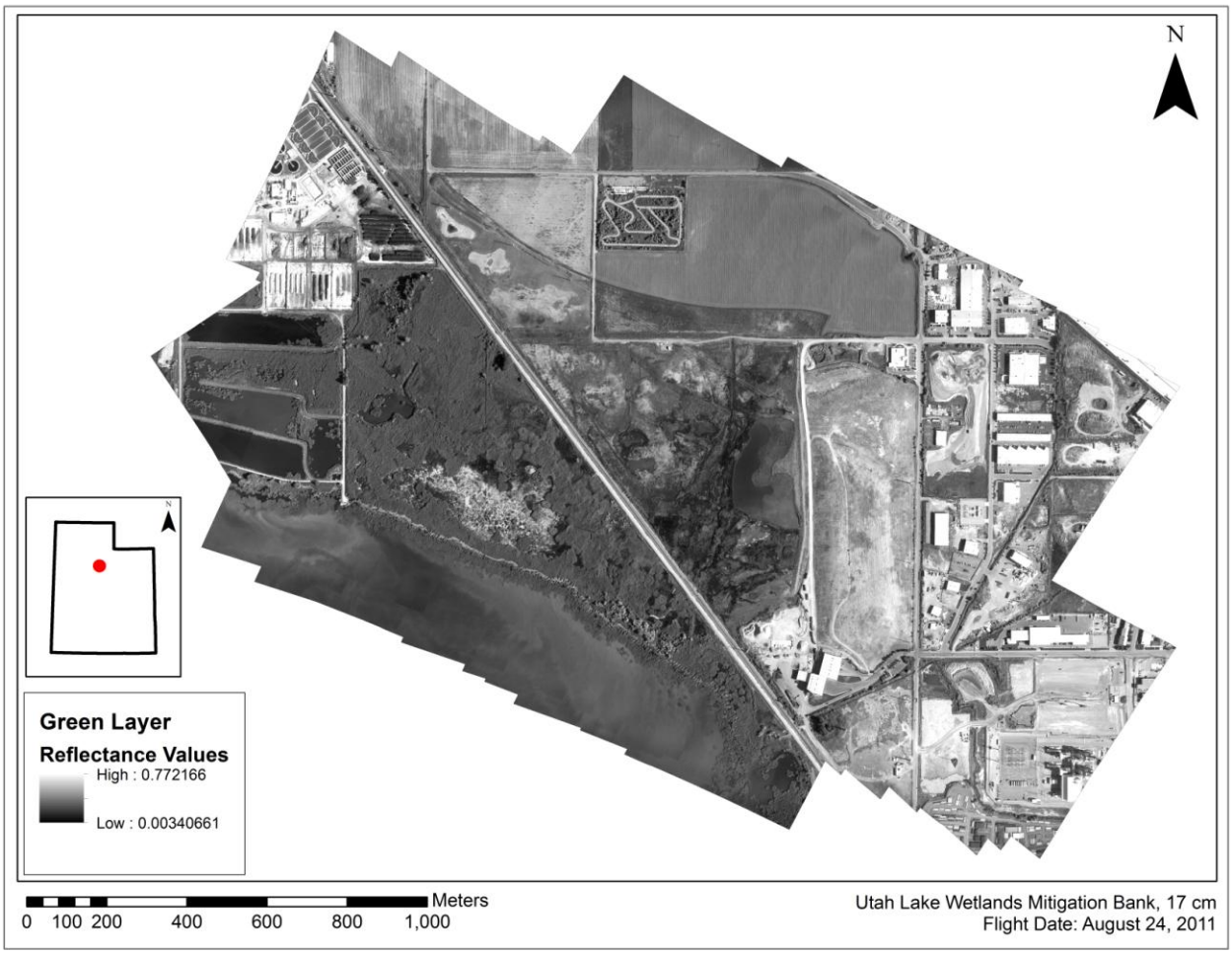

Figure 10. Green layer output from RGB reflectance value model

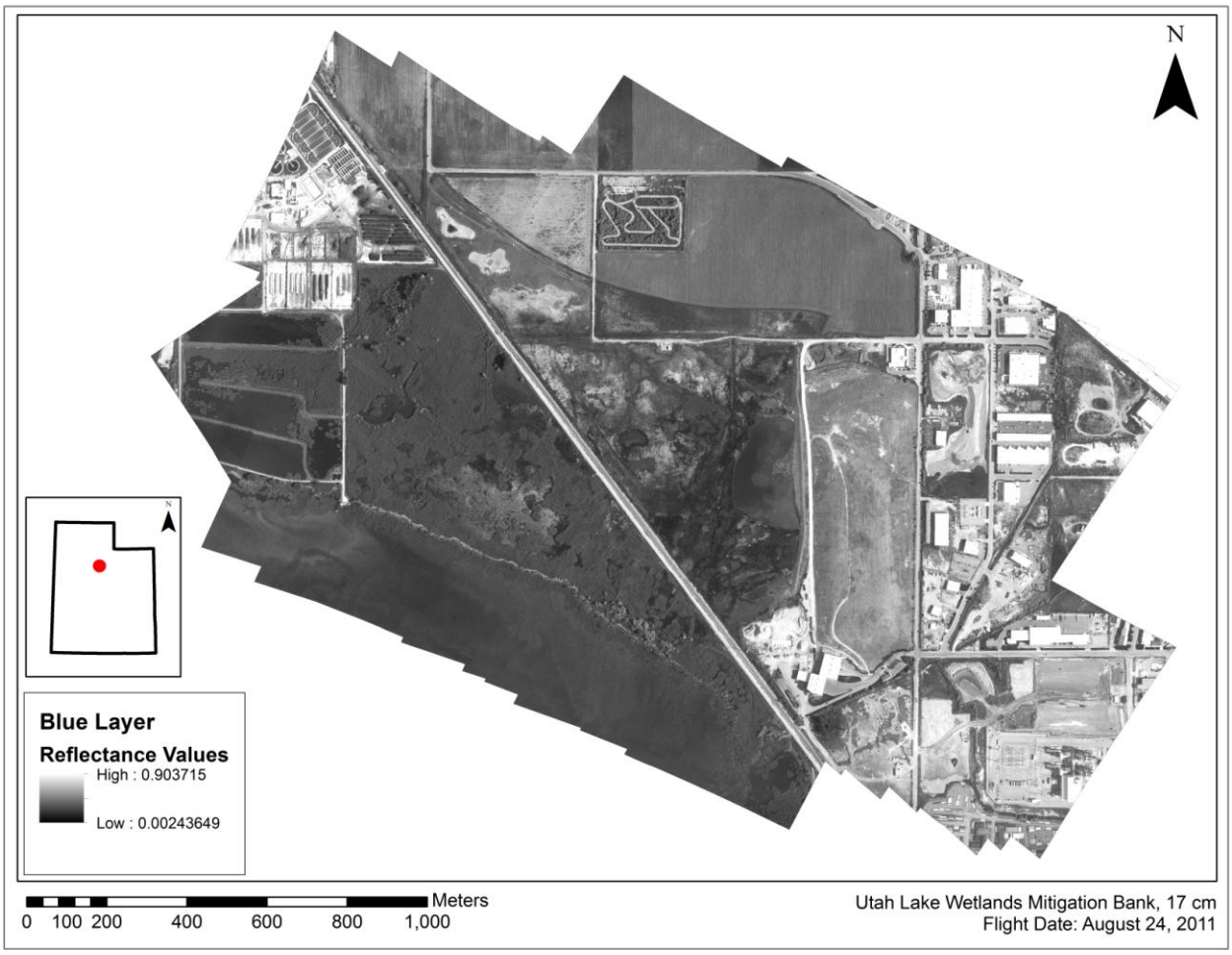

Figure 11. Blue layer output from RGB reflectance value model

2. NIR Reflectance Model

The NIR reflectance model, computed separately from the RGB model, uses the NIR orthorectified mosaic generated from a separate EnsoMosaic project. The CCD camera produces a three-band image in which the red band spectrally resembles the NIR 750 nm most closely. The red channel was separated and then divided by the NIR corrected brightness factor, which in the case of NIR imagery was the same as the correction coefficient (*CC*). The product of this model was a NIR layer with reflectance values that ranged from 0.0032 to 2.0821 (**Error! Reference source not found.**).

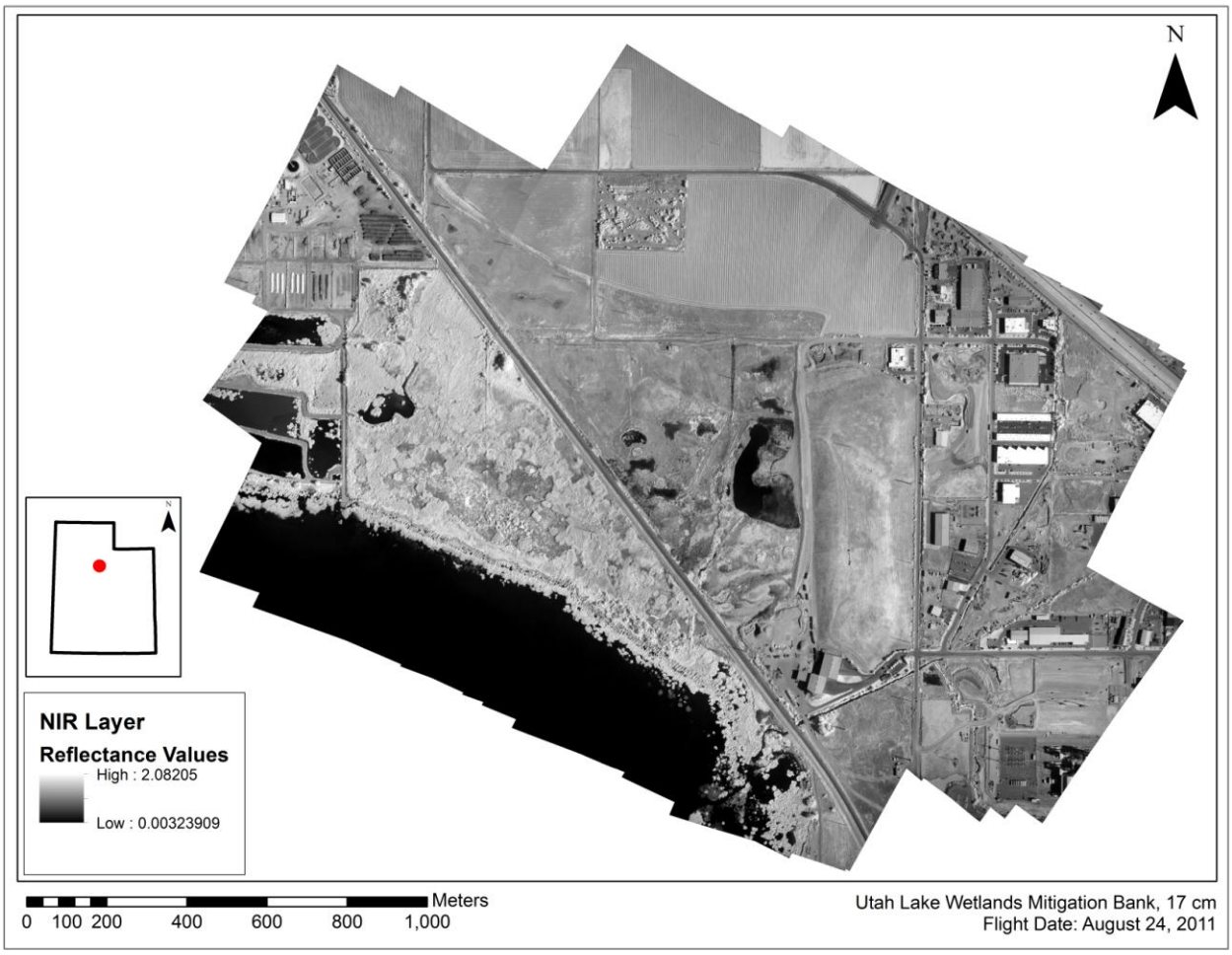

Figure 12. NIR layer in reflectance values

Once all the reflectance layers had been computed for each channel, the ERDAS Imagine Layer Stack function was used to create a four-band reflectance mosaic consisting of red, green, blue and NIR shows the resulting four-band reflectance mosaic. The reflectance mosaic was then ready for the application of various analysis techniques.

Figure 13. Four-band final reflectance image

Supervised Classification

For the Utah Department of Transportation wetland study, a fifth band was added. This was the normalized differential vegetation index (NDVI), which is the most widely accepted vegetation index for agricultural and vegetation studies (Schmaltz 2005). It uses the red and NIR bands. NDVI is robust and requires no atmospheric correction. It also reduces the impact of sunlight intensity variations, which is ideal for post mosaic classification. Calculation of the NDVI is shown in Equation 9:

$$NDVI = \frac{(NIR - RED)}{(NIR + RED)} \quad (9)$$

Using ERDAS Imagine, supervised classification was performed using the ground truth points and polygons of wetland plant species provided by UDOT on the five-band reflectance image. The plant data was divided into training and testing sets. The training set was used to create spectral signatures unique for each plant species, while the testing set was used for accuracy assessment. Although some species were spectrally similar (see Figure 14), and by ERDAS standards could have been merged, the classes were left unmerged. Otherwise, the suggested threshold merging value of 1700 for the Transformed Divergence separability function (ERDAS Field Guide 2010) would have merged all vegetation categories subsequently into one category. See Table 6 for the separability matrix for the wetland plant species.

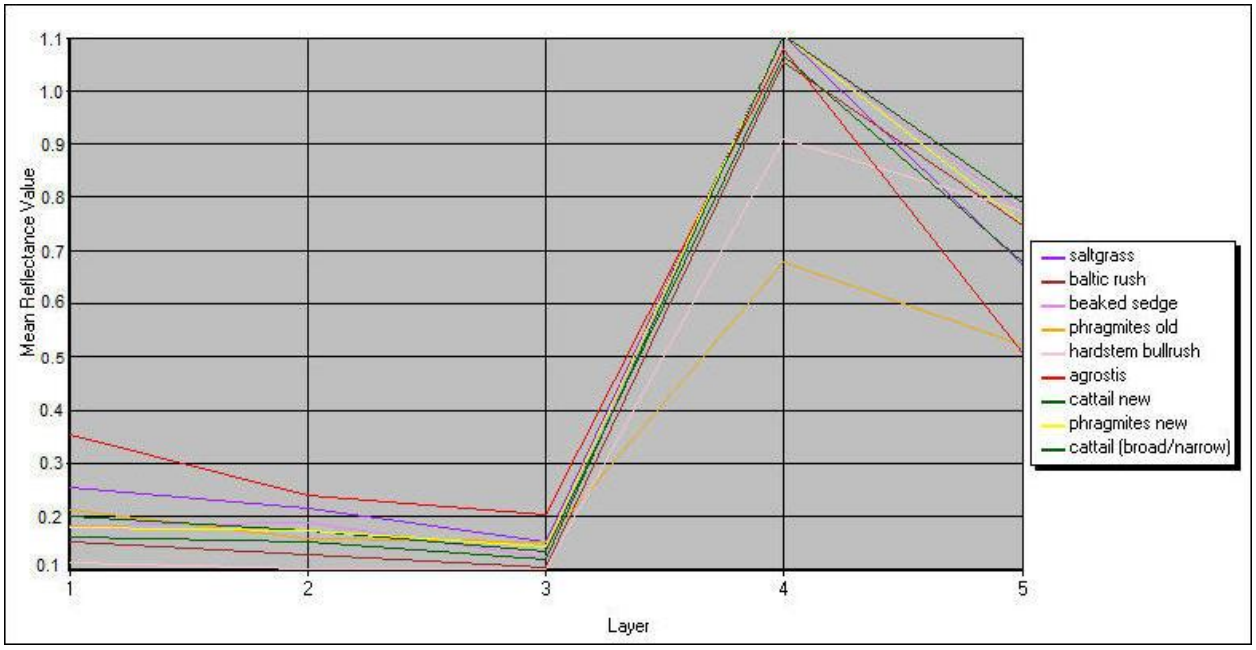

Figure 14. Mean reflectance value of defined wetland species used for supervised classification: red 1, green 2, blue 3, NIR 4 and NDVI 5

Table 6. Signature separability using transformed divergence for wetland plant species

Signature Name	1.	2.	3.	4.	5.	6.	7.	8.	9.
1. saltgrass	0	1966.18	1642.32	2000.00	2000.00	1986.35	1678.65	1814.36	1713.56
2. Baltic rush	1966.18	0	1768.65	2000.00	1495.04	2000.00	1177.86	1554.86	1623.71
3. beaked sedge	1642.32	1768.65	0	2000.00	1995.98	2000.00	1838.26	1065.14	844.14
4. *Phragmites* old	2000.00	2000.00	2000.00	0	1999.71	1998.87	1999.88	2000.00	2000.00
5. hardstem bullrush	2000.00	1495.04	1995.98	1999.71	0	2000.00	1949.92	1871.31	1920.25
6. Agrostis	1986.35	2000.00	2000.00	1998.87	2000.00	0	1987.78	1999.97	2000.00
7. cattail new	1678.65	1177.86	1838.26	1999.88	1949.92	1987.78	0	1498.36	1872.76
8. *Phragmites* new	1814.36	1554.86	1065.14	2000.00	1871.31	1999.97	1498.36	0	637.90
9. cattail (broad/narrow)	1713.56	1623.71	844.14	2000.00	1920.25	2000.00	1872.76	637.90	0

Additional signatures were added to represent roads, water, ponds, gravel, bare ground, and buildings. See Figure 15 for the Signature Editor ERDAS tool that is used for the supervised classification process. After the spectral signatures were defined, the classified image was generated using the five-band reflectance mosaic with a Maximum Likelihood classifier. A Fuzzy Convolution filter (7x7) was run to eliminate the "salt and pepper" effect of misclassified pixels. See Figure 16**Error! Reference source not found.** for the supervised classification image and legend. Cattail new, which was added to the data set later as a polygon, and the original narrowleaf/broadleaf cattail were spectrally different enough (1872.76) despite both being cattails species. UDOT asked that the narrowleaf and broadleaf cattail be merged for the study, which were originally two separate cattail species at the beginning of the project. Beaked sedge and narrowleaf/broadleaf cattail only had a spectral separability of 844.14, which suggested that these could have been merged into a unique signature under the transformed divergence guidelines. The spectral separability of *Phragmites* new, which was also added later to the data set as a polygon, and narrowleaf/broadleaf cattail was the lowest at 637.9 indicated that these two species were fairly similar.

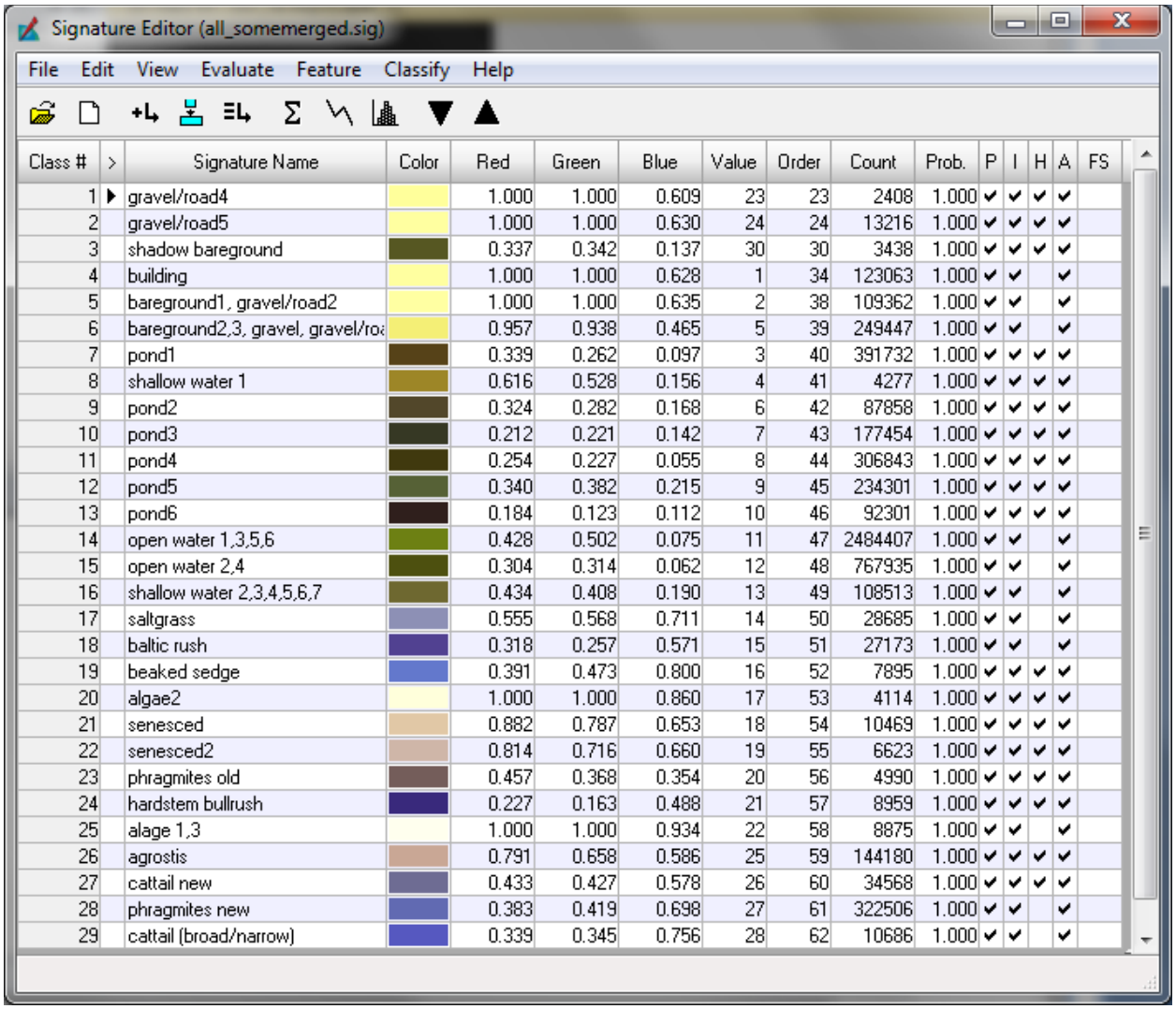

Class #	Signature Name	Color	Red	Green	Blue	Value	Order	Count	Prob.	P	I	H	A	FS
1	gravel/road4		1.000	1.000	0.609	23	23	2408	1.000	✔	✔	✔	✔	
2	gravel/road5		1.000	1.000	0.630	24	24	13216	1.000	✔	✔	✔	✔	
3	shadow bareground		0.337	0.342	0.137	30	30	3438	1.000	✔	✔	✔	✔	
4	building		1.000	1.000	0.628	1	34	123063	1.000	✔	✔		✔	
5	bareground1, gravel/road2		1.000	1.000	0.635	2	38	109362	1.000	✔	✔		✔	
6	bareground2,3, gravel, gravel/roa		0.957	0.938	0.465	5	39	249447	1.000	✔	✔		✔	
7	pond1		0.339	0.262	0.097	3	40	391732	1.000	✔	✔	✔	✔	
8	shallow water 1		0.616	0.528	0.156	4	41	4277	1.000	✔	✔	✔	✔	
9	pond2		0.324	0.282	0.168	6	42	87858	1.000	✔	✔	✔	✔	
10	pond3		0.212	0.221	0.142	7	43	177454	1.000	✔	✔	✔	✔	
11	pond4		0.254	0.227	0.055	8	44	306843	1.000	✔	✔	✔	✔	
12	pond5		0.340	0.382	0.215	9	45	234301	1.000	✔	✔	✔	✔	
13	pond6		0.184	0.123	0.112	10	46	92301	1.000	✔	✔	✔	✔	
14	open water 1,3,5,6		0.428	0.502	0.075	11	47	2484407	1.000	✔	✔		✔	
15	open water 2,4		0.304	0.314	0.062	12	48	767935	1.000	✔	✔		✔	
16	shallow water 2,3,4,5,6,7		0.434	0.408	0.190	13	49	108513	1.000	✔	✔		✔	
17	saltgrass		0.555	0.568	0.711	14	50	28685	1.000	✔	✔		✔	
18	baltic rush		0.318	0.257	0.571	15	51	27173	1.000	✔	✔		✔	
19	beaked sedge		0.391	0.473	0.800	16	52	7895	1.000	✔	✔	✔	✔	
20	algae2		1.000	1.000	0.860	17	53	4114	1.000	✔	✔	✔	✔	
21	senesced		0.882	0.787	0.653	18	54	10469	1.000	✔	✔	✔	✔	
22	senesced2		0.814	0.716	0.660	19	55	6623	1.000	✔	✔	✔	✔	
23	phragmites old		0.457	0.368	0.354	20	56	4990	1.000	✔	✔	✔	✔	
24	hardstem bullrush		0.227	0.163	0.488	21	57	8959	1.000	✔	✔	✔	✔	
25	alage 1,3		1.000	1.000	0.934	22	58	8875	1.000	✔	✔		✔	
26	agrostis		0.791	0.658	0.586	25	59	144180	1.000	✔	✔	✔	✔	
27	cattail new		0.433	0.427	0.578	26	60	34568	1.000	✔	✔	✔	✔	
28	phragmites new		0.383	0.419	0.698	27	61	322506	1.000	✔	✔		✔	
29	cattail (broad/narrow)		0.339	0.345	0.756	28	62	10686	1.000	✔	✔		✔	

Figure 15. Signature Editor tool from ERDAS

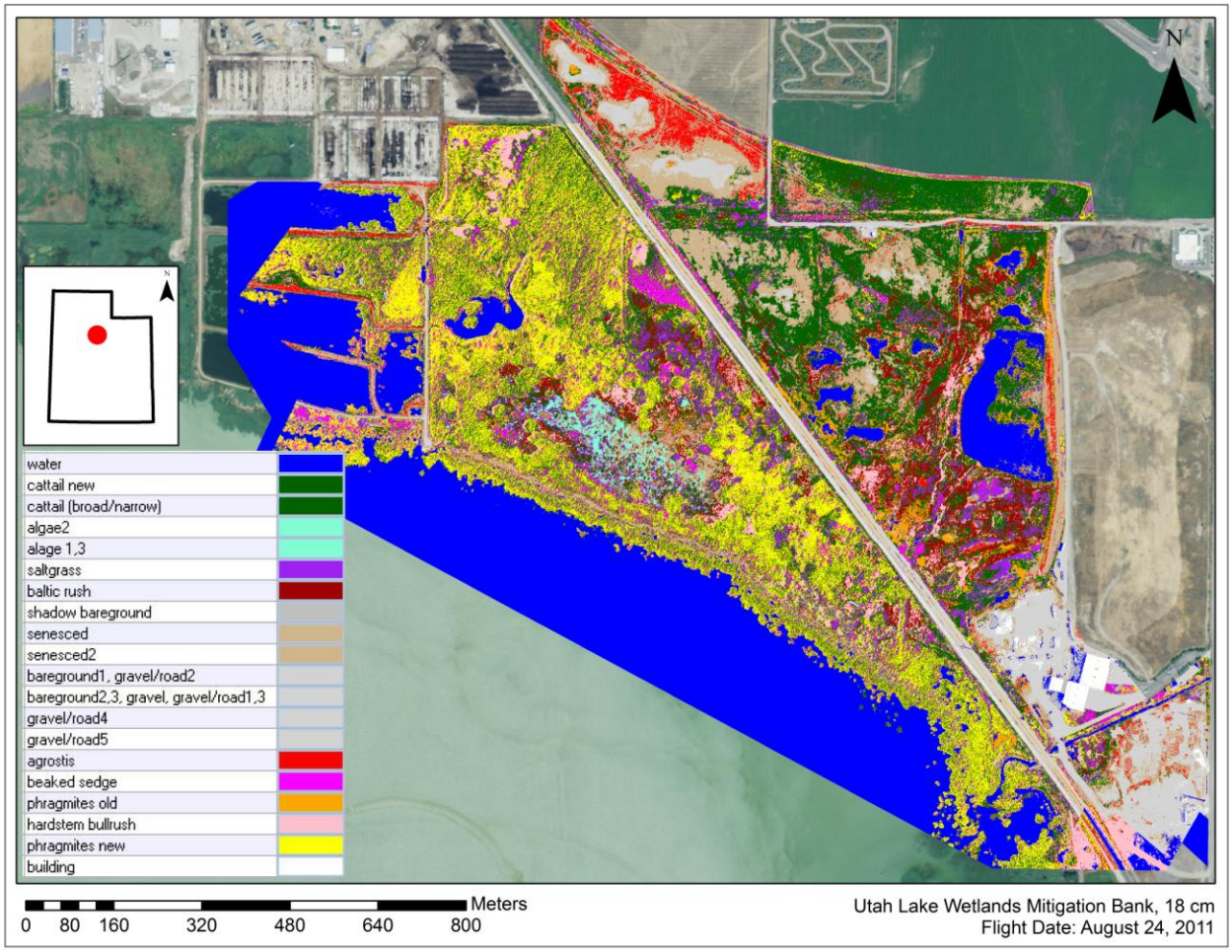

Figure 16. Supervised classification image output

RESULTS

"Accuracy assessment" is a general term for comparing the classification data to spatial data that are assumed to be true. The purpose of this comparison is to determine the accuracy of the classification process (ERDAS Field Guide 2010). The testing data set was used to determine what the pixel was defined as and how it should be classified. The results produce a *producer's accuracy* and a *user's accuracy*. The producer's accuracy is the total number of correct points in a class divided by the number of points of that class as derived from the ground truthing data and represents the probability that a pixel in a given class will have been classified

correctly on the image. The user's accuracy is the total number of correct points in a class divided by the total number of points of that class as derived from the classification data and represents the probability that a pixel classified as a particular class on the image is actually that class. The Kappa statistic indicates how well the classification results agree with the ground truth data. It conveys the "proportionate reduction in error generated by a classification process compared with the error of a completely random classification" (ERDAS Field Guide 2010). It was calculated by Table 7 shows the results of supervised classification.

Table 7. Supervised classification results of wetland species

Class Name	Reference Totals	Classified Totals	Number Correct	Producers Accuracy	Users Accuracy	Kappa Statistic
Agrostis	25	19	19	76.0%	100.0%	1.0000
Baltic rush	35	23	18	51.4%	78.3%	0.7406
cattail new	25	19	16	64.0%	84.2%	0.8214
beaked sedge	11	22	8	72.7%	36.4%	0.3295
Phragmites new	50	26	22	44.0%	84.6%	0.7998
Phragmites old	19	24	19	100.0%	79.2%	0.7716
cattail (broad/narrow)	16	43	10	62.5%	23.3%	0.1712
hardstem bullrush	15	19	13	86.7%	68.4%	0.6606
saltgrass	19	11	8	42.1%	72.7%	0.7010
Totals	216	216	133			
Overall accuracy = 61.57%						
Overall Kappa Statistic = 0.5703						

The classes that had the best classification and Kappa were *Agrostis*, Baltic rush, *Phragmites* new, *Phragmites* old, and saltgrass. Hardstem bulrush had a moderate Kappa at 0.6606, while beaked sedge and narrowleaf/broadleaf cattail had the lowest Kappa. *Phragmites* new had a fairly decent Kappa of 0.7998; however its producer's accuracy was low at 44.0%. *Phragmites* old was clearly distinguishable between other vegetation types, including *Phragmites* new, and produced a 100% producer's accuracy.

DISCUSSION

The overall accuracy of the classification was 61.57%, which indicated room for improvement (an overall accuracy of 75-100% or higher would have been ideal for a classification study). Wetland classification studies are usually a challenge due to the spectral similarities of wetland species. Although the spectral classes for each wetland species were left unmerged, according to the ERDAS Transformed Divergence suggestion of merging anything with a separability less than 1700, species could have been merged. However, after a few merges, everything would have been in one class according to the 1700 threshold. Perhaps allowing for a lower threshold for this study which would have merged some species (ie. three lowest separabilities) and others left unmerged could have improved some of the error. A few of the species had relatively low separabilities: separability for *Phragmites* new and narrowleaf/broadleaf cattail was 637.90, beaked sedge and narrowleaf/broadleaf cattail was 844.14, and *Phragmites* new and beaked sedge was 1177.86. In additional, there were other factors that may have contributed to the overall accuracy of this study.

The variations in ground truthing sampling methods may have contributed some error. Originally a set of GPS locations were used for an initial signature creation and classification. The horizontal precision of the GPS data was on average 1.058 meters. For imagery that had a pixel resolution of 0.18 meters, the GPS collected data could have been too coarse for the resolution of the imagery. If a GPS point was near the edge of a species cluster, the error could possibly have pushed it outside of the actual species boundary leading to inaccurate spectral signatures.

In addition, the hand drawn polygons sketched from Google Earth were fairly broad compared to the GPS locations. It was very likely that the polygons included other species than

included other species than what was identified. Polygon data was entered into the signature editor in its original shape, while the GPS points were added to the signature set with a seeding tool which was far more intricate method for AOIs compared to the polygons. The GPS collected data was also clustered into one area and not very well distributed among the 3.18 square kilometers of the study site which may have introduced some bias.

The areas of interest (AOIs) that were created from the GPS points were generated using the seeding/growing tool in ERDAS which searched for spectrally similar pixels based on a set of parameters. The seeding tool was quite sensitive to the slightest parameter modifications. The parameter setting was very biased and different technicians may have differencing AOIs as the parameters were determined successful by visual interpretation. Error may have been introduced in the AOI process while using highly sensitive seeding parameters and 1+ meter accuracy GPS points.

Other factors that may have contributed to the overall accuracy could have been due to the misalignment of the NIR and RGB imagery. Due to having separate cameras and camera logs from the UAV, the NIR and RGB raw imagery cannot be combined and each camera's imagery must be mosaicked separately in EnsoMosaic UAV. After the reflectance mosaic had been generated for each band, they were combined due to having the same spatial projection independent of the cameras. The RGB reflectance value images were stacked with the NIR layer using ERDAS, but the actual pixel corners were not identical causing misalignment. Despite having the same ground control points to orthorectify both the NIR and RGB mosaics in EnsoMosaic UAV, the end mosaics inherently will not be exact as each EnsoMosaic project has its own algorithmic results. Although the alignment in the Northing was accurate, there was a 6 centimeter misalignment in the Easting which could have attributed to error.

The August 24, 2011 flight represented just one snapshot of time in the wetland's growing season. Some wetland species have different spectral responses based on whether the species are emerging or receding. A multi-temporal study, having flown the UAV at other times within the growing seasons, could have improved the overall accuracy by developing a bigger picture and species patterns.

RECOMMENDATIONS FOR FURTHER RESEARCH

Continuous Panel Method vs. Modified Reflectance Mode Method

Although the modified "reflectance mode" method used by AAFC was aimed at reducing the bias in the reflectance value conversion, it would be helpful to also perform the more intensive "continuous panel" method which was the more accurate of the three methods described by Miura and Huete (2009). If a continuous panel method were performed in conjunction with the reflectance mode method for a particular study site, we could understand better the bias that is left with our method. At the moment we cannot report how much biased is reduced by adding the after-flight white panel photo.

Post-Flight Imagery Processing

The absolute normalization method was performed on orthorectified mosaics for projects conducted by the AggieAir Flying Circus at the Utah Water Research Laboratory. Due to the short flight times (~30 minutes) and low flying altitude (300-1000 meters above ground level), there was no need for atmospheric corrections and an assumed linear relationship between the digital numbers and reflectance values was justified. However, it would be more ideal to

perform the normalization method on individual images before they are used in the mosaicking software in order to produce a mosaic with minimal illumination variances between images.

Researchers at the AggieAir Flying Circus are currently working on methods for processing post-flight imagery prior to the mosaicking process. Images from the camera are converted from JPG to TIFF, and then converted into reflectance values individually by channel. EnsoMosaic UAV does not accept reflectance value images (non-8-bit form), and research is being done on a histogram scaling factor in order to be readable in EnsoMosaic UAV. The output mosaic would then be rescaled to remove the scaling factor.

Alternatively, DigiPreProcess by MosaicMill, Ltd., Finland, is a pre-processing software for UAV digital imagery that could be used prior to EnsoMosaic UAV. The goal behind DigiPreProcess is to geometrically and radiometrically improve the quality of the images in order to enable high quality mosaics, including removal of vignetting. DigiPreProcess will be investigated as an alternative for pre-mosaic image processing. The software can also convert raw CR2 Canon image formats to TIFFs, which will be convenient when the AggieAir Flying Circus upgrades to DSLR cameras.

Vignetting Correction Research

Several authors have researched the issue of vignetting correction with digital camera imagery through stand-alone mathematical models. The vignetting correction method used in this report for AggieAir is a simple straightforward method, but more complex methods have been derived. Vignetting can come from several factors: optical, mechanical, pixel and natural, and its effects increase with aperture and decrease with focal length of the camera. Various authors (Goldman et al. 2005, Zheng et al. 2006, Yu 2004) have dedicated entire papers to the

study of vignetting. If DigiPreProcess were utilized in the processing line, outside vignetting corrections would not be required.

Reflectance Panel

The barium sulfate ($BaSO_4$) panel used in this experiment has the potential to collect dust and other impurities, which can affect the reflectance properties and coefficients used in the conversion models. It is suggested that the panel be recalibrated every 2-3 months using laboratory methods described by Biggar et al. (1988) to derive new reflectance coefficients for future flights. An alternative that could save time and costs in the long run is the purchase and use of a Spectralon reflectance panel (Labsphere, Inc., North Sutton, NH, USA), which is sturdier than a $BaSO_4$ panel. A Spectralon panel can be more easily cleaned; it is more portable, and the reflectance coefficients are provided by the panel manufacturer to ensure accuracy. The current ERDAS models would be to be reassessed with the use of a Spectralon panel however.

Canon Camera Calibration

The actual spectral bandwidth of the RGB Canon PowerShot SX100 camera was unknown and unavailable from the manufacturer. It was assumed that the digital camera has a similar spectral response to that of a typical unfiltered CCD camera. AggieAir's 16-channel spectroradiometer could be used to calibrate the RGB camera in order to find the specific spectral bands (Heikkila et al. 1997). Although the exact spectral bands were not necessary for the "reflectance mode" method, it will be required for any comparison studies using data with known spectral bands such as Landsat data or if AAFC uses other reflectance conversion

methods which would require this information. Issues of image reproducibility (i.e., differences between cameras of this type) and drift have not been explored.

CONCLUSION

This paper described a method of absolute radiometric normalization used at AggieAir Flying Circus (AAFC) created for converting consumer-grade digital camera imagery into reflectance values for remote sensing applications. The method used a Canon PowerShot SX100 digital camera for the NIR and RGB as well as a barium sulfate reflectance panel with known reflectance properties. The procedure was demonstrated using imagery captured from the Utah Lake Wetlands Mitigation Bank near Pleasant Grove, Utah, which is managed by the Utah Department of Transportation for a wetlands classification study.

The method used at AAFC was adapted from Miura and Huete's (2009) "reflectance mode" method, along with equations from Crowther (1992) and Neale and Crowther (1994).. The original "reflectance mode" method from Miura and Huete (2009) used a before-flight white panel reading using a spectrometer which was then mounted on-board a UAV. The results of the spectral reflectance retrievals were biased and distorted, and also highly affected by the time of day and the length of the flight. AAFC made modifications to this method by adding an after-flight white panel photo captured in the field using the same on-board cameras used on the UAV. An average of the before and after flight data was used in the reflectance conversion which assumed a linearity due to the short flight time (30 minutes). The modifications were aimed to reduce the bias of the reflectance value conversion.

A four-band reflectance value image was generated using the method described in this paper. The overall method was very simple and could be applied to any consumer-grade digital

camera as along as a reflectance white panel with known coefficients was used in the field. While the overall accuracy from the supervised classification process had room for improvement, there were recommendations for further research which were aimed at improving the overall reflectance conversion which in turn will improve the results of a remote sensing study.

REFERENCES

Berni JAJ, Member S, Zarco-tejada PJ, Suárez L, Fereres E. Thermal and Narrowband Multispectral Remote Sensing for Vegetation Monitoring From an Unmanned Aerial Vehicle. 2009;47(3):722-738.

Biggar SF, Labed J, Santer RP, Slater PN, Jackson R, Moran MS. 1988. Laboratory calibration of field reflectance panels. Proceedings of SPIE. 1998:924, 232–240.

Crimmins MA, Crimmins TM. Monitoring plant phenology using digital repeat photography. Environmental management. 2008;41(6):949-58.

Crowther B. Radiometric calibration of multispectral video imagery. 1992. Utah State University, Dept. of Biological and Irrigation Engineering, Logan.

Dean C, Warner TA, Mcgraw JB. Suitability of the DCS460c colour digital camera for quantitative remote sensing analysis of vegetation. Science. 2000:105-118.

Duffie JA, Beckman WA. 1991. Solar Engineering of Thermal Processes. Wiley-Interscience Publication.

Goldman DB. Vignette and exposure calibration and compensation. IEEE transactions on pattern analysis and machine intelligence. 2010;32(12):2276-88.

Hardin PJ, Jensen RR. Small-Scale Unmanned Aerial Vehicles in Environmental Remote Sensing: Challenges and Opportunities. GIScience & Remote Sensing. 2011;48(1):99-111.

Heikkila J, Silvén O, Oulu I. Four-step Camera Calibration Procedure with implicit image correction. 1997:1106-1112.

Honkavaara E, Arbiol R, Markelin L, et al. Digital Airborne Photogrammetry—A New Tool for Quantitative Remote Sensing?—A State-of-the-Art Review On Radiometric Aspects of Digital Photogrammetric Images. Remote Sensing. 2009a;1(3):577-605.

Honkavaara E, Arbiol R, Markelin L, Martinez L, Bovet S, Bredif M, Chandelier L, Heikkinen V, Korpela I, Lelegard L, Pérez F, Schläpfer D, Tokola T, 2011. The EuroSDR project "Radiometric aspects of digital photogrammetric images" –Results of the empirical phase. In Proceedings of the ISPRS Hannover Workshop 2011, June 14-17, 2011, Hannover, 8 pages.

Honkavaara E, Aribol R, Markelin L, et al. Status Report of the EuroSDR Project "Radiometric Aspects of Photogrammetric Airborne Images." Finnish Geodetic Institute. 2009b.

Hurskainen P, Pellikka P. Change detection of informal settlements using multi-temporal aerial photographys – the case of Voi, of SE Kenya. Population (English Edition). 2004;(1997):17-22.

Jensen, AM, Chen YQ, Hardy T, McKee M. AggieAir - a low-cost autonomous multi-spectral remote sensing platform: New developments and applications. Proc. IEEE International Conference on Geoscience and Remote Sensing Symposium IGARSS. July 2009.

Kim SJ, Pollefeys M. Robust radiometric calibration and vignetting correction. IEEE transactions on pattern analysis and machine intelligence. 2008;30(4):562-76.

Kuusk A, Paas M. Radiometric correction of hemispherical images. ISPRS Journal of Photogrammetry and Remote Sensing. 2007;61(6):405-413.

Lebourgeois V, Bégué A, Labbé S, et al. Can Commercial Digital Cameras Be Used as Multispectral Sensors? A Crop Monitoring Test. Sensors. 2008;8(11):7300-7322.

Leica Geosystems. 2010. ERDAS Field Guide™, (7th ed.) Atlanta, Georgia.

Levin, E, Ben-Dor E, Singer A. A digital camera as tool to measure colour indices and related properties of sandy soils in semi-arid environments. International Journal of Remote Sensing. 2009;26-24: 5475–5492.

MaxMax, LLC, Carlstadt, NJ

Miura T, Huete A. Performance of Three Reflectance Calibration Methods for Airborne Hyperspectral Spectrometer Data. Sensors. 2009:9:794-813.

MosaicMill Oy. EnsoMOSAIC Image Processing User's Guide. Version 7.3. Mosaic Mill Ltd., Finland, 2009.

MosaicMill. DigiPreProcess, "http://www.mosaicmill.com/," DigiPreProcess, March 2012.

Neale CMU, Crowther B. An airborne multispectral video/radiometer remote sensing system: Development and calibration. Remote Sensing of Environment. 1994;49(3):187-194.

Neale CMU. Spring 2009. BIE 6250 - Remote Sensing of Land Surfaces, Utah State University, Logan, UT

Nebiker S, Annen A, Scherrer M, Oesch D. 2008. A Light-Weight Multispectral Sensor for Micro UAV—Opportunities for Very High Resolution Airborne Remote Sensing. The International Archives of the Photogrammetry, Remote Sensing, and Spatial Information Sciences ISPRS Congress, XXXVII, Part B1, Commission 1, 1193–1200.

Nicodemus FE, Richmond JC, Hsia JJ, Ginsberg IW, Limperis T. Geometrical Considerations and Nomenclature for Reflectance. U.S. Department of Commerce, National Bureau of Standards: Washington, D.C., 1977.

Research Systems, 2000, ENVI User's Guide, ENVI version 3.4 (Boulder: Research Systems).

Richardson AD, Jenkins JP, Braswell BH, et al. Use of digital webcam images to track spring green-up in a deciduous broadleaf forest. Oecologia. 2007;152(2):323-34.

Sakamoto T, Gitelson A, Nguy-Robertson AL, et al. An alternative method using digital cameras for continuous monitoring of crop status. Agricultural and Forest Meteorology. 2012;154-155:113-126.

Schmaltz J. 2005. Visible Earth: A catalog of NASA images and animations of our home planet. Washington, D.C.: NASA.

Swain KC, Thomson SJ, Jayasuriya HPW. Adoption of an unmanned helicopter for low-altitude remote sensing to estimate yield and total biomass of a rice crop. Transactions Of The Asabe. 2010;53(1):21-27.

Yu W. Practical anti-vignetting methods for digital cameras. IEEE Transactions on Consumer Electronics. 2004;50(4):975-983.

Zaman B. Personal communication and notes, 2011

Zheng Y, Lin S, Kambhamettu C, Yu J, Kang SB. Single-image vignetting correction. IEEE transactions on pattern analysis and machine intelligence. 2009;31(12):2243-56.

APPENDIX

CALCULATION OF SOLAR ANGLES FOR REMOTE SENSING STUDIES

Solar angles (i.e. zenith angle and azimuth angles) are required in remote sensing for establishing and reporting the bi-directional properties of natural surfaces. Also, standard reflectance panels that have been calibrated have bi-directional properties that are represented by polynomials as a function of the sun's zenith angle. Solar angles are also required to estimate the amount of energy reaching the earth's surface. The following terms and equations are defined (Duffie and Beckman, 1991):

Solar time: time associated with the angular motion of the sun across the sky and is different from the local clock time. To calculate solar time from local standard time two corrections are required. One correction for the difference in longitude between the standard and local meridians and another correction from the equation of time (E) which takes into account perturbations in the earth's rotation that affect the time the sun crosses the observer's meridian.

$$\text{Solar time} = T_{st} + 4(Lon_{st} - Lon_{loc})/60 + E/60 \quad \text{[decimalized hours]} \qquad (1)$$

Where solar time (S_t) and *local standard time (T_{st}) are in the units of [hours] on a 24 hour basis.* Equation (1) considers 4 minutes for every degree west or east of the standard meridian.

Lon_{st} is the standard meridian for the local time zone [degrees]

Lon_{loc} is the longitude of the observer or local meridian [degrees]

E is the equation of time defined as:

$$E = 9.87 \sin(2B) - 7.53 \cos(B) - 1.5 \sin(B) \quad \text{[minutes]} \qquad (2)$$

where B is

$$B = 360\,(CD - 81.25)/365 \qquad (3)$$

CD is the calendar day of the year, $1 \le CD \le 365$

Solar noon: the local standard time when the sun crosses the meridian of the observer. It can be calculated from equation (1) setting the solar time to 12:00.

Declination angle (δ): is the angular position of the sun at solar noon with respect to a plane through the equator. It varies from $-23.45° \text{ S} \le \delta \le 23.45° \text{ N}$

$$\delta = 23.45 * \sin[360/365 *(284 + CD)] \quad \text{[degrees]} \qquad (4)$$

Hour angle (ω): angular displacement of the sun east or west of the local meridian due to the rotation of the earth. Magnitude: 15° per hour, morning negative, afternoon positive.

$$\omega = (T_{st} - S_{nt})*15 \quad \text{[degrees]} \qquad (5)$$

where S_{nt} is the local time at which solar noon occurs. Or:

ω = (Solar Time – 12)* 15° [degrees] (6)

where Solar Time is the time of day in hours since midnight.

Latitude angle (Lat): angle north or south of the equator.

-90° S ≤ Lat ≤ 90° N

Longitude angle (Lon): angle west of Greenwich meridian

0° ≤ Lon ≤ 360 ° W

Zenith or incidence angle (θ): angle between a beam incident on a surface and the normal to the surface (vertical line to the zenith). The zenith or incidence angle for a horizontal surface is:

$\text{Cos}(\theta) = \sin(\delta) * \sin(\text{Lat}) + \cos(\delta) * \cos(\text{Lat}) * \cos(\omega)$ (7)

Solar Elevation Angle:

$E_s = 90 - \theta$ (8)

Surface azimuth angle (ϕ): angle between true south (in this definition) and the projection of the sun's direction onto a horizontal plane. Therefore the azimuth angle is zero at solar noon when the sun is due south (in the northern hemisphere).

-180° E ≤ ϕ ≤ 180° W

If $\cos(\omega) > \tan(\delta)/\tan(\text{Lat})$ then:

$\sin(\phi) = (\cos(\delta) * \sin(\omega))/\sin(\theta)$ (9)

If $\cos(\omega) < \tan(\delta)/\tan(\text{Lat})$ then:

$\phi = 180 - \sin^1((\cos(\delta) * \sin(\omega))/\sin(\theta))$ for western (afternoon) positions of the sun (10)

And

$\phi = -180 - \sin^1((\cos(\delta) * \sin(\omega))/\sin(\theta))$ for eastern (morning) positions of the sun (11)

Daylength:

$\text{Daylength} = 2 * ((\cos^{-1}(-\tan(\text{Lat}) * \tan(\delta)) * 180/\pi)/15)$ (12)